Insights into the material properties of dragline spider silk affecting Schwann cell migration

Aida Naghilou, Karolina Peter, Flavia Millesi, Sarah Stadlmayr, Sonja Wolf, Anda Rad, Lorenz Semmler, Paul Supper, Leon Ploszczanski, Jiliang Liu, et al.

International Journal of Biological Macromolecules 244 (2023) 125398

Contents lists available at ScienceDirect

International Journal of Biological Macromolecules

journal homepage: www.elsevier.com/locate/ijbiomac

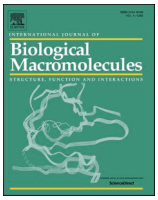

Insights into the material properties of dragline spider silk affecting Schwann cell migration

Aida Naghilou [a,b,*], Karolina Peter [c], Flavia Millesi [a,b], Sarah Stadlmayr [a,b], Sonja Wolf [a,b], Anda Rad [a,b], Lorenz Semmler [a,b], Paul Supper [a,b], Leon Ploszczanski [c], Jiliang Liu [d], Manfred Burghammer [d], Christian Riekel [d], Alexander Bismarck [e], Ellen H.G. Backus [f], Helga Lichtenegger [c], Christine Radtke [a,b]

[a] Department of Plastic, Reconstructive and Aesthetic Surgery, Medical University of Vienna, Spitalgasse 23, 1090 Vienna, Austria
[b] Austrian Cluster for Tissue Regeneration, Vienna, Austria
[c] University of Natural Resources and Life Sciences, Department of Material Sciences and Process Engineering, Institute of Physics and Materials Science, Peter-Jordan-Strasse 82, 1190 Vienna, Austria
[d] European Synchrotron Radiation Facility, 71 avenue des Martyrs, 38000 Grenoble, France
[e] University of Vienna, Faculty of Chemistry, Institute of Materials Chemistry & Research, Währingerstraße 42, 1090 Vienna, Austria
[f] University of Vienna, Faculty of Chemistry, Institute of Physical Chemistry, Währingerstraße 42, 1090 Vienna, Austria

ARTICLE INFO

Keywords:
Peripheral nerve regeneration
Trichonephila
Sterilization
Crystallinity
Secondary protein structure
Stiffness

ABSTRACT

Dragline silk of *Trichonephila* spiders has attracted attention in various applications. One of the most fascinating uses of dragline silk is in nerve regeneration as a luminal filling for nerve guidance conduits. In fact, conduits filled with spider silk can measure up to autologous nerve transplantation, but the reasons behind the success of silk fibers are not yet understood.

In this study dragline fibers of *Trichonephila edulis* were sterilized with ethanol, UV radiation, and autoclaving and the resulting material properties were characterized with regard to the silk's suitability for nerve regeneration. Rat Schwann cells (rSCs) were seeded on these silks *in vitro* and their migration and proliferation were investigated as an indication for the fiber's ability to support the growth of nerves. It was found that rSCs migrate faster on ethanol treated fibers. To elucidate the reasons behind this behavior, the fiber's morphology, surface chemistry, secondary protein structure, crystallinity, and mechanical properties were studied. The results demonstrate that the synergy of dragline silk's stiffness and its composition has a crucial effect on the migration of rSCs. These findings pave the way towards understanding the response of SCs to silk fibers as well as the targeted production of synthetic alternatives for regenerative medicine applications.

1. Introduction

Natural silk biopolymers from spiders and silkworms (*Bombyx mori*) have attracted vivid attention due to their unique properties such as mechanical stability, elasticity, biodegradability, and biocompatibility [1,2]. Particularly the dragline silk of *Trichonephila* (*T.*, previously known as *Nephila*) spiders has been used in a wide variety of applications including water collection [3], optical fibers [4], and biomedical devices [5,6]. In medical applications and tissue engineering, dragline silk's properties surpass many synthetic and natural materials [7–9]. One of the unique applications of native dragline fibers in medicine is peripheral nerve reconstruction. Currently, the prominent approach for the reconstruction of long peripheral nerve injuries is autologous transplantation [10–12]. Although recognized as the current gold-standard, this method has certain drawbacks such as donor site morbidity, limited availability, and scar formation [13–15]. An alternative is the use of nerve guidance conduits (NGCs), which have shown great potential as a viable substitute to autologous transplantation [12,16,17]. Synthetic and natural materials have been investigated for NGCs [18,19]. However, their performance is still inferior to nerve autografts for longer defects [16,17]. Hence, approaches have been developed to introduce luminal fillings such as hydrogels, fibers, and sponges in the NGCs [16,20]. The augmentation of empty conduits with dragline spider silk as a fibrous luminal filling has led to promising results [21–23]. Even for larger nerve defects of 60 mm, NGCs filled with dragline silk

* Corresponding author at: Spitalgasse 23, 1090 Wien, Austria.
E-mail address: aida.naghilou@muv.ac.at (A. Naghilou).

https://doi.org/10.1016/j.ijbiomac.2023.125398
Received 13 January 2023; Received in revised form 9 June 2023; Accepted 13 June 2023
Available online 16 June 2023

Abbreviations

Con A	Concanavalin A
FB	Fibroblast
LCI	Live cell imaging
MaSp	Major ampullate spidroins
NGC	Nerve guidance conduit
SC	Schwann cell
SEM	Scanning electron microscopy
SRO	Short-range order scattering
T.	Trichonephila
XRD	X-ray diffraction

could measure up to nerve autografts [24]. It has been shown that the success of dragline fibers can be related to their remarkable support of Schwann cell (SC) adhesion, movement, and proliferation, as well as formation of structures similar to bands of Büngner [25]. Additionally, the secondary protein structure of silk is an important aspect for guiding of the cells. The comparison of various silks from spiders highlighted that the silk with a significantly lower fraction of β-sheets conformation was unsuccessful in guiding SCs, leading to cell agglomerations [26].

Recently, studies have also focused on tailoring the properties of natural and synthetic silk materials. Hydration was shown to alter the crystallinity, mechanical properties, and secondary protein structures of spider and silkworm silks [27–30]. The impact of simple treatment methods, such as sterilization on structures made of silkworm's fibroin proteins was investigated with the aim of enhancing the degradation rate [31–34]. It was observed that ethanol and autoclaving of recombinant and regenerated silk-based materials affect secondary protein structures significantly, increasing the β-sheet content and by that decreasing the degradation rate. UV radiation could as well impact the properties of silk depending on the exposure time [35,36].

Spider silk is derived from a non-sterile source, therefore sterilization is necessary to prevent bacterial and fungal growth [37]. However, the impact of sterilization methods on silk biopolymers is mostly limited to regenerated silk fibroins of silkworms. In addition, although spider silk is a template for the production of advanced materials in nerve regeneration, the effect of sterilization on the fiber is not yet systematically studied. Furthermore, even though the high β-sheet content is firmly established to be a prerequisite for the use of silks in tissue engineering, little is known on how the increased β-sheet content after sterilization affects the synergistic material properties of silk and by that the response of cells.

Hence, in this work, dragline silk of *T. edulis* has been sterilized with ethanol, UV radiation, and autoclaving. These methods were chosen as previous studies on silkworm fibroins have demonstrated that ethanol and autoclaving have a significant effect on the protein structures, while UV radiation hardly affects the silk. Thus, during *in vitro* studies the UV silk can be employed as a control for the native fibers, as the unsterilized silk cannot be used *in vitro* [37]. Therefore, the effect of various sterilization methods on native spider dragline silk can be determined and insights on the material properties of the fibers supporting nerve regeneration are provided. In addition, tailoring of silk's functionality by unambiguous and routine methods such as sterilization could be achieved.

The dragline silk of *T. clavipes* is reported to be composed of two core layers of major ampullate spidroins (MaSp) 1, 2, and 3 [38], and a shell consisting of a skin, a glycoprotein layer, and an outmost lipid coat [39,40]. It can be expected that *T. edulis* has a similar layered morphology. Each of these five components may affect cell behavior. Hence, in the current work, material characterization of the silk fibers spanned over multiple levels, covering a micrometer to nanometer range. Fiber morphology was studied by scanning electron microscopy (SEM) and staining of concanavalin A (con A) protein [39], secondary protein structures by Raman spectroscopy [41,42], crystallinity by X-ray diffraction (XRD) [43], and mechanical properties by tensile testing [44]. In addition, we quantified the response of dragline silk to SCs, which are crucial for nerve regeneration [45–47]. Rat SCs (rSCs) were seeded on silk fibers and cultured. The behavior of cells was evaluated by live cell imaging (LCI) and proliferation assays [25].

2. Materials and methods

2.1. Spider silk harvesting and sterilization

The dragline silk from adult female *T. edulis* was harvested with a reeling speed of 8 mm s^{-1} adapting the procedures published in Ref [48]. The silk was reeled on a 1 cm^2 frame (stainless steel) with 15 rotations on each axis. For sterilization, commonly used procedures were used:

- Immersion in ethanol [32,33]: The silk was immersed in 70 % ethanol for 15 min. Afterwards, they were air-dried for 2 h under sterile conditions.
- UV radiation [37,49]: The silk was irradiated for 45 min with a Hg lamp (Osram) emitting UV light at the dominant wavelength of 254 nm and a power of 12 W. All silks were placed at the same distance from the light source to ensure reproducible radiation.
- Autoclaving [32,48]: The silk was autoclaved with a LABOKLAV instrument. For this process, air was saturated with water vapor at a temperature of 121 °C and a pressure of 1 bar. These conditions were maintained for 15 min followed by cooling to room temperature. This temperature was chosen, as thermogravic measurements have shown that heating below 140 °C does not affect the silk significantly [50].

2.2. Isolation and seeding of rat Schwann cells

Male and female adult Sprague Dawley rats (10–14 weeks of age) were used as organ donors in this study. The animals were euthanized according to the Austrian's Animal Testing Law (TVG 2012, §2, 1.c) and the Article 3 of the Directive 2010/63/EU of the European Parliament and of the Council on the Protection of Animals Used for Scientific Purposes [51].

Established protocols were used to isolate and culture rSCs [26,52]. Details on the isolation and culturing conditions can be found in the supplementary material. rSCs cultures in passages 3–6 (p3-p6) from 5 individual donors ($n = 5$) were used. 15×10^4 rSCs in a volume of 10 μl were seeded on suspended dragline silk and kept at 37 °C and 5 % CO_2 for 1 h. Afterwards, the silk and the silk frames were submerged in growth medium. The cultures were inspected daily by phase contrast optical microscopy (NIKON Eclipse Ts2R) for signs of bacterial or fungi growth.

2.3. Live cell imaging

LCI was started 3 h after seeding of rSCs. For this, an Olympus IX83 microscope with a 10×/0.3 objective was used. A built-in incubator kept the cells at 37 °C and 5 % CO_2 during imaging. Every 10 min a phase contrast micrograph was taken at multiple positions on each condition for a total of 20 h. Afterwards, the videos were manually evaluated, and 25 rSCs per condition were randomly chosen in the beginning of video and tracked. A custom evaluation algorithm was devised with Wolfram Mathematica, allowing the calculation of distances and velocities. However, as cells could cover large distances on the silk, in multiple cases the randomly chosen rSCs exited the frame covered by the microscope objective. Therefore, to allow a conclusive and unbiased comparison that also takes the faster cells into consideration, only the rSC velocities were compared between conditions. In this way, the

values are independent of the total time that a rSC has been tracked. Two quantities were evaluated in these experiments, the total and the effective (Euclidean) velocity.

2.4. Immunofluorescence staining and confocal microscopy

After 14 days of cultivation, 10 μM 5-ethynyl-2deoxyuridine (EdU) was added and the cultures were kept at 37 °C and 5 % CO_2 for 22 h. Then, immunofluorescence staining of rSCs was performed based on procedures described elsewhere [25]. The cells were stained for SC marker S100 and cell marker vimentin. Nuclei were stained with 4′,6-diamidino-2-phenylindole (DAPI) solution. The staining procedure is described in the supplementary material. For quantitative analysis of the purity and proliferation of rSCs, the cells were manually counted and assessed. A minimum of 200 cells positive for DAPI ($DAPI^+$) were taken into consideration. Cells positive for S100 and vimentin ($S100^+$/$vimentin^+$) were evaluated as rSCs, cells negative for S100 and positive for vimentin ($S100^-$/$vimentin^+$) as rat fibroblasts (rFB), and rSCs positive for EdU ($S100^+$/$vimentin^+$/EdU^+) as proliferating rSC.

In addition to immunofluorescence staining of rSCs, the silk itself was also investigated by staining of the con A protein. This protein is found in the outer parts of dragline silk and can be an indication of the layered morphology of the fiber [39]. Native silk and the fibers after sterilization with ethanol, UV radiation, and autoclaving were stained. Silk fibers in their native form without staining were used to assure the lack of autofluorescence in the chosen wavelength range of the con A staining. For staining, all silks were placed in a permeabilization and blocking solution containing 1× Dulbecco's phosphate-buffered saline (1× PBS) 1 % bovine serum albumin (BSA, SIGMA), 5 % goat serum (GS, DAKO) for 30 min. After washing with 1× PBS, they were incubated in 1 mg/ml con A detection solution (Thermo Fisher) in 1× PBS with 1 % BSA and 1 % GS for 2 h. Afterwards, Fluoromount-G mounting medium was added, and the silks were stored at 4 °C.

All immunofluorescence images were obtained with a Leica SP8 confocal microscope, using a 20×/0.75 multi-immersion objective.

2.5. Scanning electron microscopy

A Zeiss Supra 55 VP scanning electron microscope was employed, and the micrographs were obtained with a secondary electron detector at 10^{-5} mbar. The silk was coated with a 10 nm gold layer by means of a Leica SDC050 sputter coater equipped with a quartz micro balance to confirm the layer thickness. The diameter of the silks was evaluated manually using the image analyzing software Smart TIFF.

2.6. Raman spectroscopy

A WITec alpha 300A micro-Raman device and a 100×/0.9 objective were used. Measurements were performed on suspended single silk fibers with a frequency doubled Nd:YAG laser at a wavelength of 532 nm, an average power of 10 mW, and acquisition time of 5 min. The silk showed no morphological alterations under these conditions. The spectra were collected in backscatter geometry with a resolution of 2 cm^{-1}.

The secondary protein structure of dragline silk possesses a directionality [41,53]. Hence, the molecular orientation was investigated by recording four polarized spectra: The polarization of the incoming laser light was oriented either parallel (z) or perpendicular (x) to the long axes of silk and a polarizer before the detector allowed the detection of scattered signal also in z and x direction. Hence measurements in xx, xz, zx, and zz orientations were acquired. These measurements were performed on three spots of two fibers, leading to six spectra for each condition. Spectra were corrected for the fluorescent background with a polynomial function.

Afterwards for each spot, the orientation insensitive spectrum (isotropic, I_{iso}) was calculated and the quantification of the secondary protein structures was performed by spectral decomposition of the conformation sensitive amide I regions and the side chains (1550–1750 cm^{-1}) of the isotropic spectra [41]. More information on the isotropic spectra calculation and the spectral decomposition is provided in the supplementary material.

2.7. X-ray diffraction (XRD)

X-ray nanodiffraction (XRD) was carried out at The European Synchrotron (ESRF, Grenoble, France) at beamline ID 13 with a synchrotron radiation beam of $\lambda = 0.08157$ nm wavelength, focused to about 200 nm spot at the position of single or double silk fibers deposited on X-ray transparent Si_3N_4 membranes [43]. Mesh-scans were performed normal to and along the fiber axis with 200 nm × 500 nm step-increments at ambient conditions. Diffraction patterns were recorded at each step by a single photon counting pixel detector. More detail about the procedure can be found in the supplementary material.

Peaks in the XRD patterns were indexed for the β-poly(L-Ala) structure [54,55] with a doubled *a*-axis. Bragg peaks and diffuse scattering (SRO for short-range order scattering) were fitted with Gaussians and non-linear least squares fitting. Pixels at non-sensitive detector areas were excluded from the fit. The lattice spacings (*d*[hkl]) were derived by azimuthally integrating the data and plotting the corresponding intensity against q ($q = 4\pi sin\Theta\lambda^{-1} = 2\pi d^{-1}$, where 2Θ is the Bragg angle, λ is the wavelength, and d is the lattice spacing). The crystalline domain size along certain (hkl) lattice directions (L[hkl]) was calculated from the full-width-at-half-maximum of the Gaussian fitted Bragg peaks according to Scherrer's Eq. [56]. The degree of crystallinity was calculated by the total area under the Bragg peaks divided by the sum of the area under the Bragg peaks and diffuse scattering. The unit cell parameters *a* (interchain), *b* (intersheet), and *c* (chain direction) of the orthorhombic poly(L-Ala) structures were calculated based on the reflections (210), (020), and (002), respectively [57]. The uncertainties were calculated based on the Gaussian peak fits.

2.8. Tensile testing

The tensile properties of the silk were measured using a FAVIMAT single fiber testing device from Textechno equipped with a 210 cN load cell. The gauge length was set to 3 cm, and the tests were performed at a 3 mm min^{-1} speed. Experiments were carried out at 25 °C and 30 % humidity.

Silk strands were carefully removed from the silk frame and cut with scissors. To ensure straight suspension of the silk in the device, a clamp with a weight of 43 mg was attached to one end of the fiber and the silk was hung vertically between the two grips of the device. After the measurements, the fibers were inspected by SEM and results for double silk strands were discarded, leading to eight single fibers measured per condition. Smart TIFF software was used to measure the diameter the silk fiber from the SEM images at six points on areas away from fibers' end to avoid artefacts caused by clamping. Circular cross sections were assumed and the average diameters were employed for the calculation of stress from the force values. The elastic modulus (*E*-modulus) was determined from the linear region at 0.2 % strain [58]. The breaking stress and maximum strain at failure were also analyzed.

2.9. Statistical analysis

The data are represented as mean and standard deviations. The normality of data's distribution was verified by means of quantile-quantile plots and for the *in vitro* experiments, a two-way ANOVA approach allowing the comparison of experimental conditions independent of the donors was used [59,60]. For the material characterization experiments, an unequal variance *t*-test was employed for the statistical evaluation. As the XRD experiments were performed at The European Synchrotron with limited allocated beam time, not enough

data points could be measured to justify a statistical analysis. Hence, no statistical tests were performed for this experiment.

3. Results

The applied methods resulted in sterility of the silks. The growth media stayed clear, and no presence of fungi or bacteria could be observed by phase contrast microscopy of the rSC cultures on the silks during the 14 days of cultivations. Hence, the proliferation and migration of rSCs could be investigated on the sterilized silks as the unsterilized native fibers cannot be integrated in the *in vitro* experiments [37].

3.1. Schwann cell purity and proliferation

To determine the extent of cellular proliferation on silk, multicolor staining and confocal microscopy were employed. Fig. 1, column 1 and 2 depict the merged and DAPI stainings, respectively. The positive staining for SC marker S100 (Fig. 1, column 3) together with the small amount of $S100^{-}$/$vimentin^{+}$ (Fig. 1, column 4) cells indicated the high purity of rSC cultures on all silks. In fact, no significant differences between the purity in the conditions and cultures consisting of over 95 % rSCs were found (Fig. 1d). rSCs proliferated on all fibers (Fig. 1, column 5). The proliferation rates are shown in Fig. 1e. Although there is a trend of lower proliferation on UV radiated and autoclaved fibers in comparison to ethanol treated ones, no statistically significant differences were detected.

3.2. Schwann cell velocity

LCI was employed to quantify the migration of rSCs on sterilized

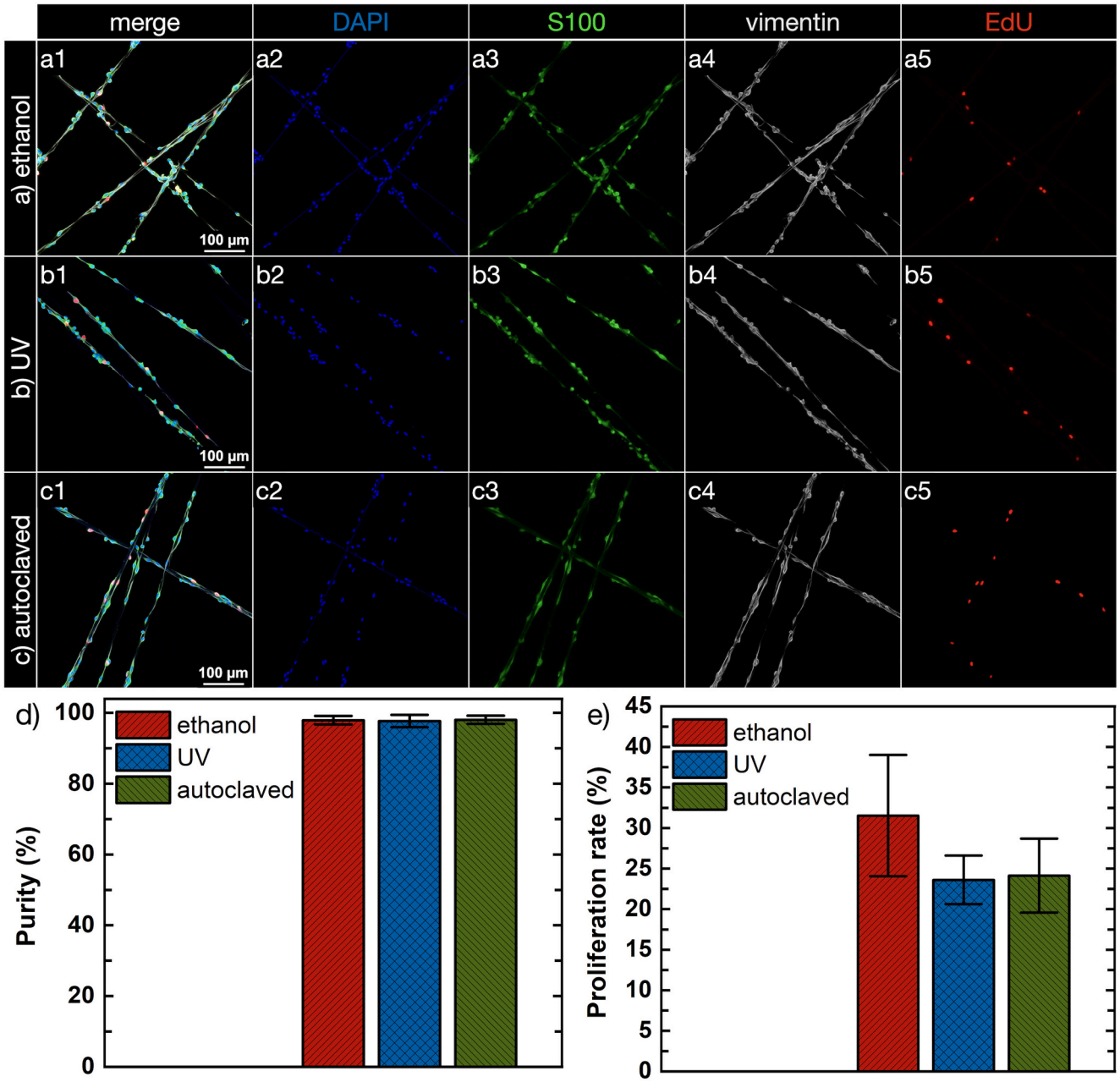

Fig. 1. Purity and proliferation of rSCs on silk. Immunostaining micrographs of rSCs on dragline silk of *T. edulis* sterilized with a) ethanol, b) UV radiation, and c) autoclaving. Merged channels (column 1), DAPI in blue (column 2), S100 in green (column 3), vimentin in gray (column 4), and EdU proliferation marker in red (column 5). The quantification d) purity and e) proliferation of the cultures ($n = 5$). No significant differences between the rSC cultures on the fibers were detected.

dragline fibers. Fig. 2 a-c depicts the phase contrast micrographs of rSCs attached to silk fibers. Each image is superimposed with the tracking results of five cells shown as colored lines. The total velocity of the cells is significantly higher for the silk sterilized with ethanol in comparison to the other methods (Fig. 2 d). The UV radiation in turn, supports a significantly faster movement of rSCs when compared to autoclaving. In addition, the effective velocity, which defines the change in location is significantly lower for autoclaved silks in comparison to the ethanol treated fibers. A diagram depicting the donor dependent effective velocity of rSC on the autoclaved silk in comparison to the ethanol treated fibers for statistical analysis is shown in supplementary Fig. S1.

3.3. Silk morphology

SEM images revealed the size and morphology of the silks. The micrographs (Fig. 3 a-d) showed no visible morphological changes between the native dragline and sterilized fibers. All silks showed a smooth and featureless topography. The diameter of the fibers evaluated from the SEM images indicated insignificant variations between the sizes (supplementary Fig. S2). Hence, the sterilization methods did not cause irreversible shrinkage or expansion of the silk matrix. Similarly, other silk-inspired materials such as fibroin scaffolds previously described in literature demonstrated no significant pore size change before and after sterilization [32].

To further understand the influence of sterilization on the layered morphology of the fibers, con A staining was employed. This staining can show the impact of sterilization on the outer layers of spider silk, as this protein is found in the glycoprotein layer and with a smaller content in the skin layer [39]. Staining after sterilization showed remarkable differences. While the significant smaller fluorescence signal after treatment with ethanol indicates that both the glycoprotein layer and the skin layer were almost completely removed (Fig. 3 f), both layers are clearly intact after UV radiation and autoclaving (Fig. 3 g, h). The observed intense spots, also visible on the native silk, could be due to the presence of glycoprotein aggregates. This inhomogeneity of the outer layer of the silk is most likely due to the staining process, as such aggregates were not observed under the electron microscope.

3.4. Secondary protein structure

In order to assess the impact of sterilization on the molecular structure and conformation of the silk, Raman spectroscopy was performed. Supplementary Fig. S3 depicts the average Raman spectra of native, as well as treated silks for xx, xz, zx, and zz measurements. Quantitative evaluation of the peaks can be found in supplementary material. For the quantification of the secondary protein structures, the orientation insensitive spectra were calculated from the polarized spectra as described in supplementary material and shown in Fig. 4 a for the amide I region. The autoclaved silk has the largest deviation in comparison to the native silk, while the spectral width of the ethanol treated silk is also smaller. Spectral decomposition was performed to quantify the conformation of the secondary protein structures. An example of the fitting procedure for the native silk is shown in Fig. 4 b. The averages and standard deviations for the results of the fits are shown in Fig. 4 c. Both autoclaving and ethanol treatment increased the β-sheet content and decreased the content of helices on dragline silk similar to studies on silk fibroin of silkworm [31–34]. UV radiation, minimally decreased the content of β-sheets. This insignificant change with radiation is in-line with previous studies [61].

3.5. Ultrastructure

Fig. 5 depicts the XRD results of the dragline fibers in native state and after sterilization. The black arrow in the diffraction patterns (top row) shows the direction of the silk's long axis. The dashed black lines enclose the integration area. The corresponding radial equatorial intensity profiles and the best fits are depicted in Fig. 5 bottom row. An example of the meridional intensity profile showing the fit of the (002) Bragg peak for the native silk is depicted in supplementary Fig. S4.

A combination of the Bragg peaks (hkl indices) corresponding to the poly(L-Ala) lattice, and SRO scattering ascribed to the glycine-rich domains is noticeable in Fig. 5 [62]. Clear differences between the native silk fibers and after ethanol treatment and autoclaving are visible. Indeed, the prominence of (020) Bragg peaks for the ethanol treated and autoclaved silks can be attributed to a relative reduction in SRO peak intensity suggesting an increase in crystallinity, which is due to the higher β-sheets content [63,64]. In addition, the (040) peak is only clearly visible for the ethanol treated and autoclaved silks. The fibers exposed to UV radiation on the other hand, appear practically unchanged in comparison to the native silk.

Table 1 shows the unit cell parameters of the orthorhombic poly(L-Ala) lattice. The values are in good agreement with previously reported data for *Nephila* and other orb waving spiders except for a smaller c-axis parameter for autoclaved silk [62,65].

In accordance with the results of Raman spectroscopy, which showed an increase in the crystalline β-sheet content for ethanol treated and autoclaved silks, the degree of crystallinity derived from the XRD measurements is greater in these two fibers (Fig. 6 a). The crystalline domain size (L) also shows that in the (020) lattice direction all values of L are similar to the native fiber, while an increase for ethanol treated and autoclaved silks in the (210) lattice direction was detected (Fig. 6 c, d). As the (210) lattice direction is a mixed index of intersheet and interchain direction (see Fig. 6 b), it can be deduced that the change in domain size of ethanol treated and autoclaved fibers in (210) lattice direction is mainly caused by a change in interchain direction (since there is no difference visible in intersheet direction). This means that by ethanol treatment and autoclaving of the silk the crystalline domains of β-sheets in interchain lattice direction increased in size. An explanation could be newly formed hydrogen bonds, reducing the content in amorphous domains. Interestingly, although both silks show larger crystalline

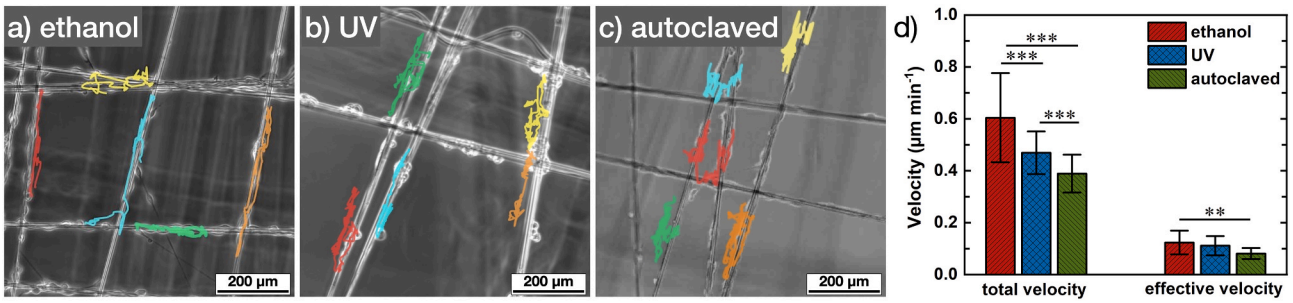

Fig. 2. Live cell imaging micrographs and velocity. Representative phase contrast images of rSCs on spider silk fibers sterilized with a) ethanol b) UV radiation, and c) autoclaving. Each image is superimposed with the tracking results of five cells shown as the colored lines. d) Quantification of rSCs' total and effective velocity after 20 h ($n = 5$). **: p-value <0.01, ***: p-value <0.001.

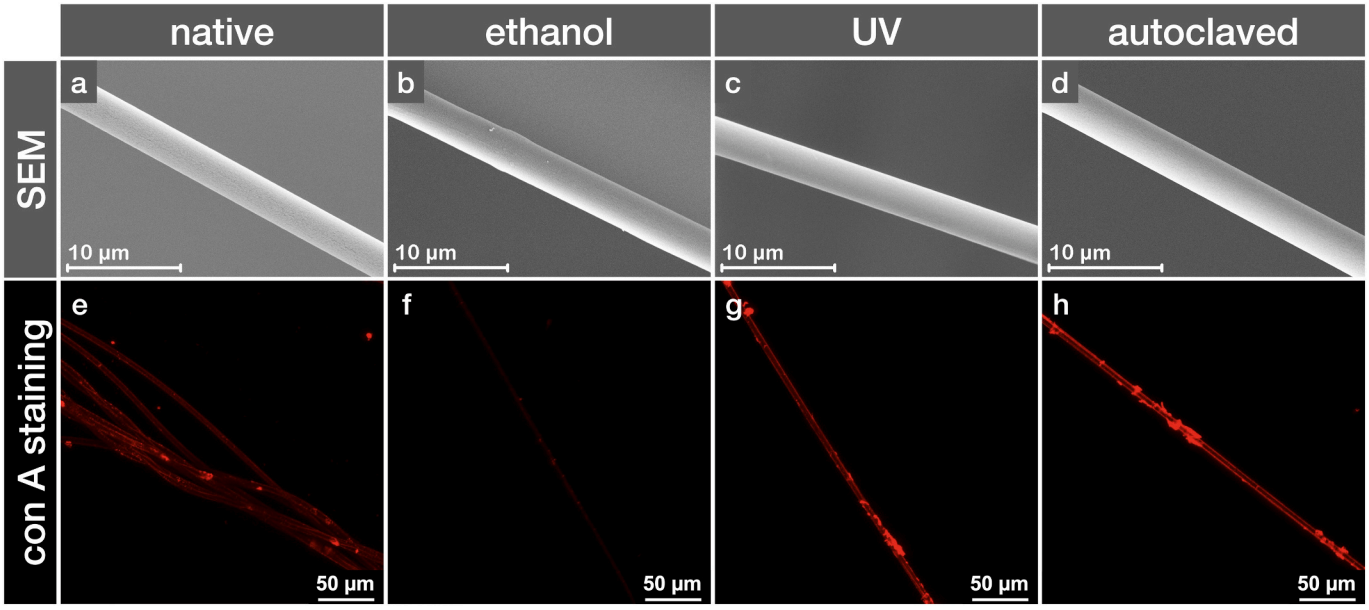

Fig. 3. Scanning electron micrographs of spider silk for a) dragline silk of *T. edulis* in native state and after sterilization with b) ethanol, c) UV radiation, and d) autoclaving. No significant variation in morphology or diameter was observed. Immunostaining micrographs of dragline silk of *T. edulis* stained for con A protein e) native silk and after sterilization with f) ethanol, g) UV radiation, and h) autoclaving.

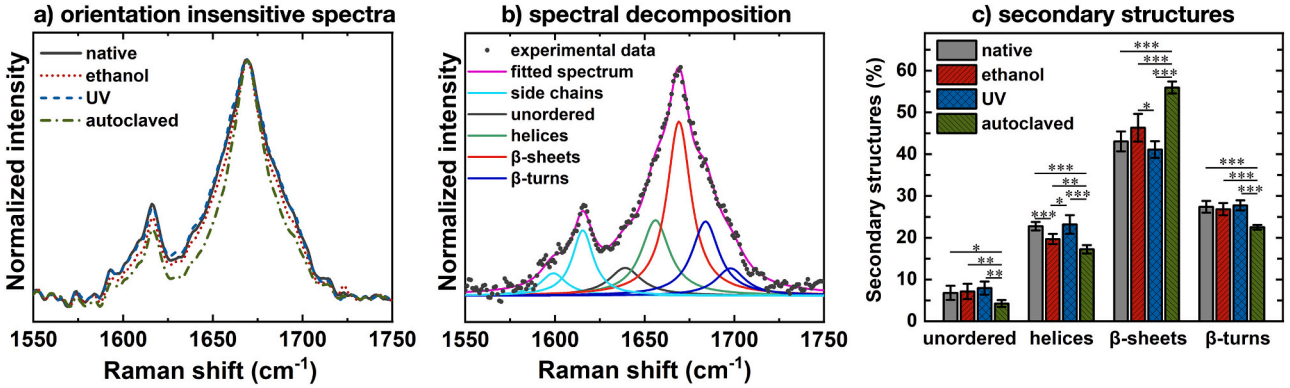

Fig. 4. a) Average of 6 orientation insensitive Raman spectra in amide I region for the dragline silk of *T. edulis* in native state and after sterilization with ethanol, UV radiation, and autoclaving. For better comparability, the spectra were normalized to least square deviation from the native silk in the 1550–1750 cm^{-1} range. b) An example of the spectral decomposition of the amide I region for the native silk. c) The content of secondary protein structures calculated from the fit of orientation insensitive spectra. *: *p*-value <0.05 **: p-value <0.01, ***: p-value <0.001.

domains in interchain lattice direction, the lattice spacing (*d*) differs. Compared to native silk, ethanol treated silk shows a slightly larger lattice spacing in (020) direction and smaller lattice spacing in (210) direction, indicative of an increase in lattice spacing by ethanol treatment in intersheet direction and a decrease in lattice spacing in interchain direction. On the other hand, autoclaving of silk only leads to an increased lattice spacing in intersheet direction and no effect in interchain direction can be observed. The c-axis parameters of native, ethanol and UV-treated fibers are similar (Table 1) and close to Pauling's ideal antiparallel β-sheet value of 0.700 nm [66]. The c-axis value for the autoclaved sample of 0.677 nm is, however, shorter but does not reach 0.650 nm suggested by Pauling&Corey for a parallel-chain packing [66]. There is also no evidence for transition to a parallel chain packing in Raman spectra. To conclude, ethanol treatment and autoclaving result in larger crystalline domains in interchain direction and for autoclaved silk a slightly larger distance between the β-sheets (Fig. 6 e). In case of ethanol treatment, this also goes hand in hand with slightly more compact arrangement of the molecular chains (Fig. 6 f). Overall, the differences in lattice spacing are very small compared to the changes in crystalline domain size in the corresponding lattice directions (notice the scale on the y-axes in Fig. 6e and f). Therefore, the largest effect of the sterilization procedures (ethanol treatment and autoclaving) is likely to be the increase in size of the crystalline domains in interchain direction as well as the increased crystallinity. UV radiation does not cause a significant change in crystal structure based on these results.

3.6. Tensile properties

Fig. 7 a depicts the representative stress strain curves of the silks, while Fig. 7 b-d, show their *E*-moduli, breaking stress, and strain at failure, respectively. The mechanical properties showed variabilities, typical for the native silk fibers [67]. Nevertheless, while the breaking stress and strain at failure have large variations for each fiber, the E-moduli are more uniform. In addition, the E-modulus of the native silk is in good agreement with previous experiments on *T. edulis* fibers, independent of the different reeling speed, relative humidity, and measurement specifications while breaking stress is lower [58,68,69]. The *E*-modulus is a materials property less dependent on material flaws,

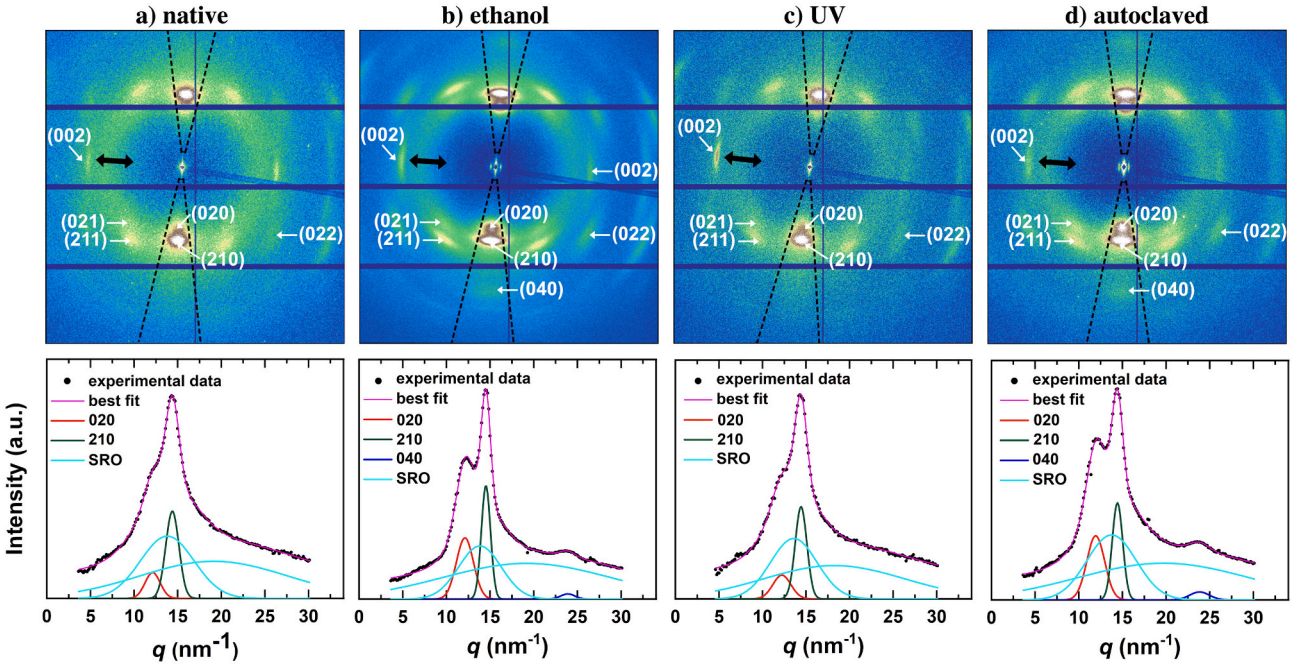

Fig. 5. Diffraction patterns and intensity profiles of dragline silk fibers of *T. edulis* in a) native state and after sterilization with b) ethanol c) UV radiation, and d) autoclaving. The black arrow shows the direction of the silk's long axis. The dashed black lines enclose the integration area.

Table 1
Unit cell parameters for the orthorhombic poly(L-Ala) lattice.

	Interchain, *a* (nm)	Intersheet, *b* (nm)	Chain direction, *c* (nm)
Native	0.964 ± 0.001	1.037 ± 0.004	0.685 ± 0.001
Ethanol	0.953 ± 0.001	1.038 ± 0.002	0.682 ± 0.001
UV	0.967 ± 0.002	1.029 ± 0.006	0.686 ± 0.0005
Autoclaved	0.962 ± 0.001	1.053 ± 0.002	0.677 ± 0.001

including those introduced by handling of the fibers. However, the lower breaking stress can be explained by these defects. The silk fibers were reeled throughout this study on the same frames to allow the correlation between *in vitro* studies and material characterizations. The rectangular shape of the frames necessary for the *in vitro* experiments could introduce flaws, especially kinks, in the fiber, reducing its breaking strength.

The fiber modulus increased after autoclaving as visible in Fig. 7b. Similar findings were reported for compression modulus of autoclaved scaffolds fabricated from the silk fibroin of *Bombyx mori* [32,34]. As E-modulus is dependent on the crystallinity [70], the higher modulus values for the autoclaved silk are in-line with the Raman results, displaying the largest increase in β-sheet content for the autoclaved fibers. In contrast, no clear trend was found in breaking stress or maximum strain of the sterilized fibers in comparison to the native silk.

4. Discussion

In search for the optimum luminal filling for NGCs, the success of the dragline silk of spider genus *Trichonephila* was confirmed [24,71]. In fact, the dragline fibers were capable of bridging a critical length gap of 60 mm, which has not been achieved with other materials [72]. For the use in biomedical applications, a crucial part is the sterilization of biopolymers, whether native or recombinant [37]. Previous studies have mostly focused on the effect of various sterilization methods on degradation rates of silk-inspired materials and less on relating the material properties after sterilization to the cell response. The motivation is that, by elucidating the underlying mechanisms leading to the successful support of cells by spider silk, design of silk-inspired materials with specific properties leading to desired cellular response will be possible. These properties certainly have to be investigated for the intended function of the biomaterial for a specific cell type [33]. Hence, in this work, established parameters of velocity and proliferation rate of SCs on silk were used as indications for the suitability of sterilization methods (treatment with ethanol, UV radiation, and autoclaving) in nerve regeneration applications [25].

All sterilized fibers in this study were successful in guiding rSCs and no visible differences in cell alignment along the fibers were observed. In addition, the cells proliferated on all silks with some minor but not significant variations between the conditions. Nevertheless, rSCs were faster and moved further on ethanol treated fibers in comparison to autoclaved ones. On UV radiated fibers, the cells were slower than ethanol treated silk but faster than rSCs on the autoclaved fibers.

For elucidating the reasons for the different velocities, silks' topography was investigated as it is an essential factor in cell attachment, alignment, migration, and growth [73–77]. SC movement is especially sensitive to substrate morphology and it has been shown that electrospun gelatin fibers with larger diameters lead to higher effective velocities of SCs [78]. However, the size and roughness of the silks in our study were comparable based on the SEM data, and an effect of these parameters on rSC velocity can be excluded.

Secondary protein structures strongly affect the mechanical properties of silk fibers. Crystalline β-sheets contribute to the fiber's tensile strength, while the amorphous matrix of helical structures, as well as β-turns result in the fiber's extensibility [41,79]. The decomposition of the orientation insensitive Raman spectra enabled us to conclude that UV radiation hardly affected the secondary protein structures. However, both ethanol treatment and autoclaving increased the β-sheets content in comparison to the native dragline silk. Hence, the faster movement of rSCs on ethanol treated fibers in comparison to autoclaved ones cannot be solely attributed to the increase in β-sheets content (which was observed for both, ethanol and autoclave treatment) and may be related to other aspects. The XRD data in our study demonstrated differences in the ultrastructure of the fibers. While both ethanol treatment and autoclaving led to larger crystalline domains in-line with Raman spectroscopy results, as well as larger lattice distances in the interchain direction, the molecular chain of β-sheets were slightly compacter in ethanol treated fibers, which may also affect the mechanical properties.

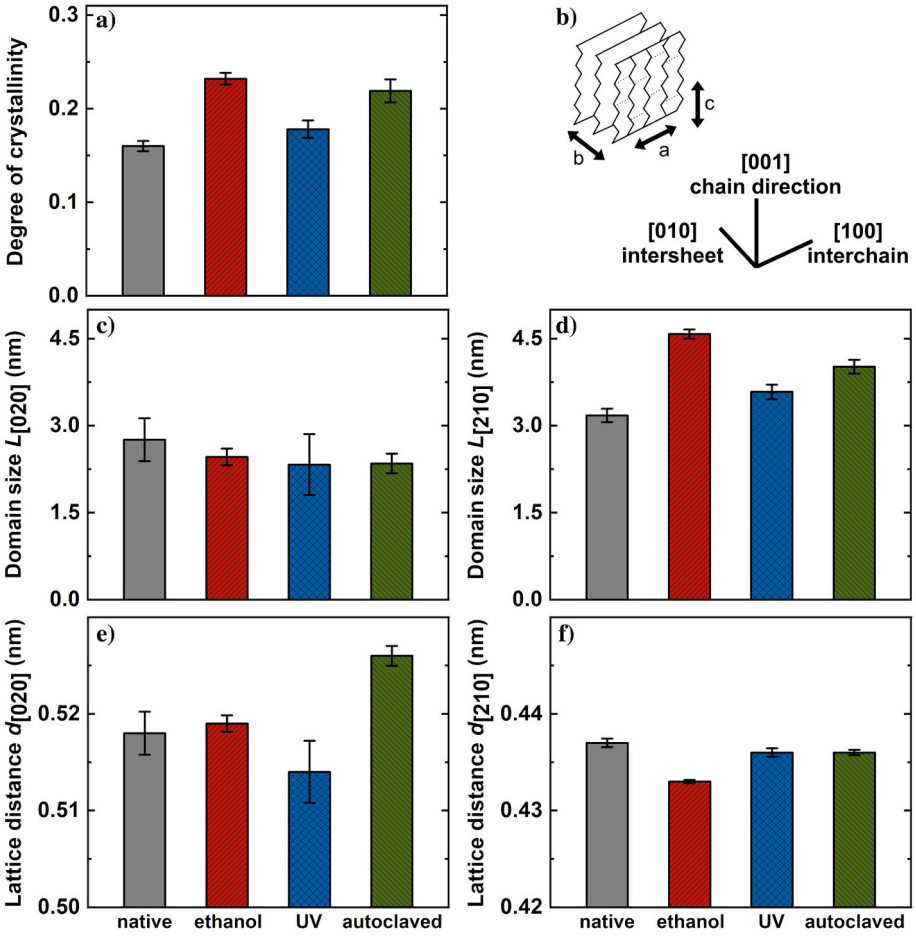

Fig. 6. a) Degree of crystallinity, b) schematic of lattice directions c) crystalline domain size [020] d) crystalline domain size [210] e) lattice distance [020] f) lattice distance [210] of the dragline silk of *T. edulis* in native state and after sterilization with ethanol, UV radiation, and autoclaving.

Tensile tests demonstrated that the autoclaved silk was significantly stiffer than the other three fibers, which could be explained by the highest content of crystalline β-sheets as seen by Raman spectroscopy. This could be the reason for the slower migration of rSCs on autoclaved silk as SCs are strongly mechanoreceptive and stiffness variations affect their velocity [80,81]. However, the stiffness of ethanol treated fibers and those exposed to UV radiation were similar, yet rSCs on fibers submerged in ethanol had a higher total velocity and a similar effective velocity as the UV radiated ones.

Hence, other effects such as surface chemistry cannot be excluded. It is of-note, that the effect of the outer layers of dragline silk on cells has never been investigated before this study. The staining of con A protein, present in the skin and glycoprotein layers of silk fibers showed that ethanol treatment mostly removes both these layers, as the con A protein was barely detected by staining. It is unlikely that SC migration is directly affected by this removal, as the migration is shown to be affected by myelin-associated glycoproteins [82] and not the glycoproteins related to spidroins which are found in dragline silk [39]. In addition, the missing outer layers do not affect the stiffness of fibers either, which is also in-line with previous studies [83]. Nevertheless, the partial removal of these layers may indirectly impact the rSC migration, as it allows better access of the cells to the core layer of the silk containing the MaSp proteins. It is believed, that the Gly-Arg-Gly-Gly-Leu motif in MaSp1, which is a binding sequence for neural cell adhesion molecules is crucial for the support of nerve regeneration by spider silk [84]. Hence, more contact to the core layer could be responsible for the faster movement of rSCs on ethanol treated silk, as they are in direct contact with the Gly-Arg-Gly-Gly-Leu motif.

Based on this comprehensive study our interpretation is that not one property, but a synergy of multiple characteristics of spider silk substrates governs the migration of rSCs. The removal of skin and glycoprotein layers together with the stiffness of fibers are found to be the major aspects of SCs-dragline silk interactions. The significant higher stiffness of the autoclaved silk and the removal of the shell layer of the ethanol treated fibers, giving access to the inner layers, could be expected to have caused the high migration velocity of rSCs on the latter. These results are encouraging for the field of recombinant silk, as the outer layers of dragline silk are not present when producing synthetic silk fibers. Our findings show that these layers are in fact not necessary and a fiber comparably successful as the natural silk in nerve regeneration can be produced as long as the other necessary material characteristics to sustain SCs proliferation and migration are met.

5. Conclusions

In this work, the reasons behind the success of dragline silk of spider *T. edulis* in supporting rSCs were investigated. The fibers were sterilized and compared based on their material properties and the ability to support rSCs. The results demonstrated that rSCs had similar purity and proliferation rates on all silks. However, they had a higher total and effective velocity on ethanol treated dragline fibers and were slowest on autoclaved ones. While the silk's size after sterilization remained practically the same as the native fibers, the β-sheet content and thus the crystallinity of the dragline silk increased significantly for the ethanol treated and autoclaved fibers. The stiffness was also found to be highest for the autoclaved silk. In addition, the treatment with ethanol led to an

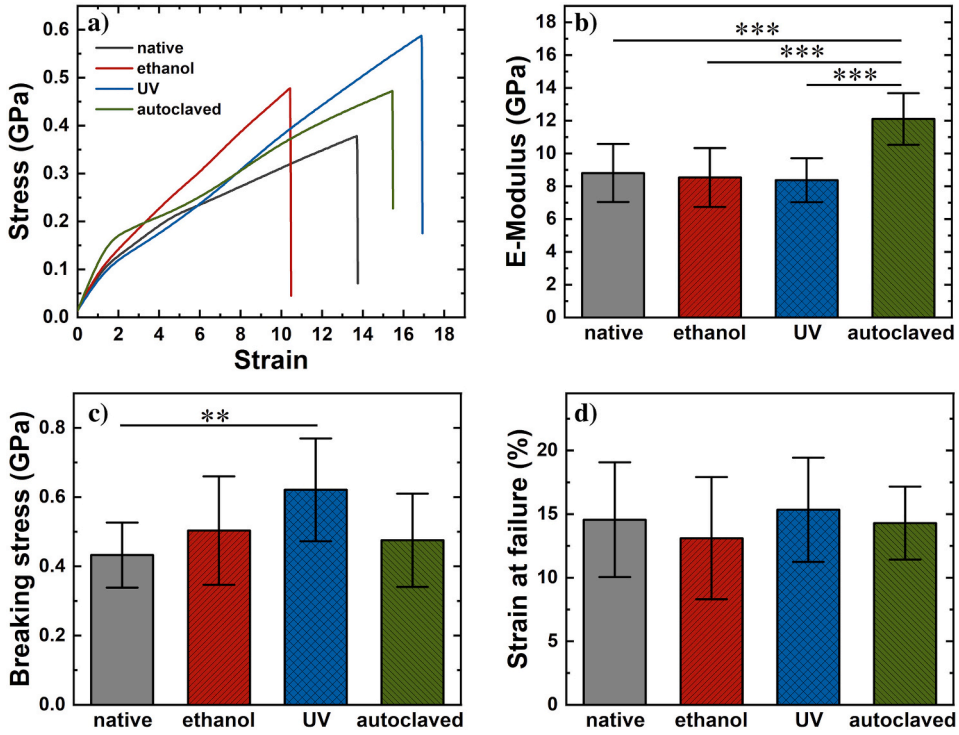

Fig. 7. a) Representative stress strain curves b) E-modulus c) breaking stress, and d) strain at failure of eight measurements on the dragline silk of *T. edulis* in native state and after sterilization with ethanol, UV radiation, and autoclaving. **: *p*-value <0.01, ***: p-value <0.001.

almost complete removal of the outer layers of the silk, giving the cells better access to the fiber's core. Hence, it is suggested that the higher stiffness of the autoclaved silk slowed down rSCs, while the removal of glycoprotein and skin layers of the silk positively affected the faster migration and directionality of rSCs. The results provide essential insights that can be used for targeted production of tailored silk-based materials specifically for nerve regeneration applications.

Supporting information

Additional details for SC isolation, velocity, and staining, Raman spectroscopy, SEM, and XRD.

CRediT authorship contribution statement

Aida Naghilou: Conceptualization, Data curation, Formal analysis, Funding acquisition, Investigation, Methodology, Project administration, Resources, Software, Supervision, Validation, Visualization, Writing – original draft, Writing – review & editing. **Karolina Peter:** Data curation, Formal analysis, Investigation, Methodology, Software, Validation, Visualization, Writing – original draft, Writing – review & editing. **Flavia Millesi:** Conceptualization, Formal analysis, Investigation, Methodology, Resources, Validation, Writing – review & editing. **Sarah Stadlmayr:** Data curation, Formal analysis, Investigation, Methodology, Resources, Validation, Visualization, Writing – review & editing. **Sonja Wolf:** Data curation, Investigation, Methodology, Writing – review & editing. **Anda Rad:** Data curation, Investigation, Methodology, Writing – review & editing. **Lorenz Semmler:** Methodology, Resources, Writing – review & editing. **Paul Supper:** Methodology, Resources, Writing – review & editing. **Leon Ploszczanski:** Data curation, Investigation, Writing – review & editing. **Jiliang Liu:** Data curation, Formal analysis, Investigation, Methodology, Software, Validation, Writing – review & editing. **Manfred Burghammer:** Data curation, Formal analysis, Investigation, Methodology, Software, Validation, Writing – review & editing. **Christian Riekel:** Data curation, Formal analysis, Investigation, Methodology, Software, Validation, Writing – review & editing. **Alexander Bismarck:** Methodology, Supervision, Validation, Writing – review & editing. **Ellen H.G. Backus:** Methodology, Supervision, Validation, Writing – review & editing. **Helga Lichtenegger:** Methodology, Project administration, Funding acquisition, Supervision, Validation, Writing – review & editing. **Christine Radtke:** Methodology, Project administration, Funding acquisition, Supervision, Validation, Writing – review & editing.

Declaration of competing interest

The authors declare that they have no known competing financial interests or personal relationships that could have appeared to influence the work reported in this paper.

Data availability

Data will be made available on request.

Acknowledgments

The authors would like to thank Dr. Stephan Puchegger and the faculty center for nanostructure research at the University of Vienna for support with scanning electron microscopy as well as Professor Bruno K. Podesser and his team at the Center for Biomedical Research, Medical University of Vienna for sharing euthanized rats for tissue harvest. We are grateful for the constant support from Dr. Marion Gröger and her team at the Core Facility Imaging of Medical University of Vienna. The XRD experiments were performed on beamline ID13 at the European Synchrotron Radiation Facility (ESRF), Grenoble, France. We are grateful to Manfred Burghammer at the ESRF for providing assistance in using beamline ID13. We also thank Dr. Robyn Plowright from Newrotex Ltd. for partly providing the silks employed for the revisions.

This research is supported by the Austrian Science fund (FWF): project number P 33613.

Appendix A. Supplementary data

Supplementary data to this article can be found online at https://doi.org/10.1016/j.ijbiomac.2023.125398.

References

[1] F. Schäfer-Nolte, K. Hennecke, K. Reimers, R. Schnabel, C. Allmeling, P. Vogt, J. Kuhbier, U. Mirastschijski, Biomechanics and biocompatibility of woven spider silk meshes during remodeling in a rodent fascia replacement model, Ann. Surg. 259 (2014) 781–792.

[2] N. Johari, A. Khodaei, A. Samadikuchaksaraei, R.L. Reis, S.C. Kundu, L. Moroni, Ancient fibrous biomaterials from silkworm protein fibroin and spider silk blends: biomechanical patterns, Acta Biomater. 153 (2022) 38–67.

[3] Y. Zheng, H. Bai, Z. Huang, X. Tian, F.-Q. Nie, Y. Zhao, J. Zhai, L. Jiang, Directional water collection on wetted spider silk, Nature 463 (2010) 640–643.

[4] Z.H. Liu, M. Zhang, Y. Zhang, Y. Xu, Y.X. Zhang, X.H. Yang, J.Z. Zhang, J. Yang, L. B. Yuan, Spider silk-based tapered optical fiber for humidity sensing based on multimode interference, Sensors and Actuators a-Physical 313 (2020) 5.

[5] K.Y. Chun, S. Hyeong Kim, M. Kyoon Shin, C. Hoon Kwon, J. Park, Y. Tae Kim, G. M. Spinks, M.D. Lima, C.S. Haines, R.H. Baughman, S. Jeong Kim, Hybrid carbon nanotube yarn artificial muscle inspired by spider dragline silk, Nat. Commun. 5 (2014) 3322.

[6] M.S. Sidhu, B. Kumar, K.P. Singh, The processing and heterostructuring of silk with light, Nat. Mater. 16 (2017) 938–945.

[7] T.B. Aigner, E. DeSimone, T. Scheibel, Biomedical Applications of Recombinant Silk-Based Materials 30 (2018) 1704636.

[8] S. Salehi, K. Koeck, T. Scheibel, Spider silk for tissue engineering applications, Molecules 25 (2020) 20.

[9] F. Millesi, T. Weiss, C. Radtke, Silk biomaterials in peripheral nerve tissue engineering, in: J. Phillips, D. Hercher, T. Hausner (Eds.), Peripheral Nerve Tissue Engineering and Regeneration, Springer International Publishing, Cham, 2020, pp. 1–29.

[10] H.J. Seddon, Nerve grafting, Ann. R. Coll. Surg. Engl. 32 (1963) 269–280.

[11] B.J. Pfister, T. Gordon, J.R. Loverde, A.S. Kochar, S.E. Mackinnon, D.K. Cullen, Biomedical engineering strategies for peripheral nerve repair: surgical applications, state of the art, and future challenges, Crit. Rev. Biomed. Eng. 39 (2011) 81–124.

[12] C. Radtke, Natural occurring silks and their analogues as materials for nerve conduits, Int. J. Mol. Sci. 17 (2016) 1754.

[13] R. Birch, Surgical Disorders of the Peripheral Nerves, Springer-Verlag, London, 2011.

[14] C.M. Nichols, M.J. Brenner, I.K. Fox, T.H. Tung, D.A. Hunter, S.R. Rickman, S. E. Mackinnon, Effects of motor versus sensory nerve grafts on peripheral nerve regeneration, Exp. Neurol. 190 (2004) 347–355.

[15] S.E. Mackinnon, A.R. Hudson, Clinical application of peripheral nerve transplantation, Plast. Reconstr. Surg. 90 (1992) 695–699.

[16] X. Jiang, S.H. Lim, H.-Q. Mao, S.Y. Chew, Current applications and future perspectives of artificial nerve conduits, Exp. Neurol. 223 (2010) 86–101.

[17] A.M. Moore, R. Kasukurthi, C.K. Magill, H.F. Farhadi, G.H. Borschel, S. E. Mackinnon, Limitations of conduits in peripheral nerve repairs, HAND 4 (2009) 180–186.

[18] A. Magaz, A. Faroni, J.E. Gough, A.J. Reid, X. Li, J.J. Blaker, Bioactive silk-based nerve guidance conduits for augmenting peripheral nerve repair, Adv Healthc Mater 7 (2018), e1800308.

[19] T. Kornfeld, P.M. Vogt, C.J.W.M.W. Radtke, Nerve grafting for peripheral nerve injuries with extended defect sizes 169, 2019, pp. 240–251.

[20] M.B. Chen, F. Zhang, W.C. Lineaweaver, Luminal fillers in nerve conduits for peripheral nerve repair, Ann. Plast. Surg. 57 (2006) 462–471.

[21] C. Allmeling, A. Jokuszies, K. Reimers, S. Kall, C.Y. Choi, G. Brandes, C. Kasper, T. Scheper, M. Guggenheim, P.M. Vogt, Spider silk fibres in artificial nerve constructs promote peripheral nerve regeneration, Cell Prolif. 41 (2008) 408–420.

[22] C. Allmeling, A. Jokuszies, K. Reimers, S. Kall, P.M. Vogt, Use of spider silk fibres as an innovative material in a biocompatible artificial nerve conduit, J. Cell. Mol. Med. 10 (2006) 770–777.

[23] F. Roloff, S. Strau, P.M. Vogt, G. Bicker, C. Radtke, Spider silk as guiding biomaterial for human model neurons, J BioMed Research International 2014 (2014), 906819.

[24] C. Radtke, C. Allmeling, K.-H. Waldmann, K. Reimers, K. Thies, H.C. Schenk, A. Hillmer, M. Guggenheim, G. Brandes, P.M. Vogt, Spider silk constructs enhance axonal regeneration and Remyelination in long nerve defects in sheep, PLoS One 6 (2011), e16990.

[25] F. Millesi, T. Weiss, A. Mann, M. Haertinger, L. Semmler, P. Supper, D. Pils, A. Naghilou, C. Radtke, Defining the regenerative effects of native spider silk fibers on primary Schwann cells, sensory neurons, and nerve-associated fibroblasts, FASEB J. 35 (2021), e21196.

[26] A. Naghilou, L. Pöttschacher, F. Millesi, A. Mann, P. Supper, L. Semmler, T. Weiss, E.H.G. Backus, C. Radtke, Correlating the secondary protein structure of natural spider silk with its guiding properties for Schwann cells, Mater. Sci. Eng. C 116 (2020), 111219.

[27] J. Dionne, T. Lefèvre, P. Bilodeau, M. Lamarre, M. Auger, A quantitative analysis of the supercontraction-induced molecular disorientation of major ampullate spider silk, Phys. Chem. Chem. Phys. 19 (2017) 31487–31498.

[28] D. Stengel, J.B. Addison, D. Onofrei, N.U. Huynh, G. Youssef, G.P. Holland, Hydration-induced β-sheet crosslinking of α-helical-rich spider prey-wrapping silk, Adv. Funct. Mater., n/a 2007161.

[29] Y. Liu, Z. Shao, F. Vollrath, Relationships between supercontraction and mechanical properties of spider silk, Nat. Mater. 4 (2005) 901–905.

[30] T. Asakura, M. Endo, Y. Tasei, T. Ohkubo, T. Hiraoki, Hydration of Bombyx mori silk cocoon, silk sericin and silk fibroin and their interactions with water as studied by 13C NMR and 2H NMR relaxation, J. Mater. Chem. B 5 (2017) 1624–1632.

[31] Y. Wang, X. Zhang, J. Brugger, Fabrication and Characterization of Biodegradable, Thermal-Responsive Silk Composite Membrane, 2018 IEEE 13th Annual International Conference on Nano/Micro Engineered and Molecular Systems (NEMS), 2018, pp. 479–482.

[32] E.S. Gil, S.-H. Park, X. Hu, P. Cebe, D.L. Kaplan, Impact of sterilization on the enzymatic degradation and mechanical properties of silk biomaterials, Macromol. Biosci. 14 (2014) 257–269.

[33] S. Hofmann, K.S. Stok, T. Kohler, A.J. Meinel, R. Müller, Effect of sterilization on structural and material properties of 3-D silk fibroin scaffolds, Acta Biomater. 10 (2014) 308–317.

[34] J. Rnjak-Kovacina, T.M. DesRochers, K.A. Burke, D.L. Kaplan, The effect of sterilization on silk fibroin biomaterial properties, Macromol. Biosci. 15 (2015) 861–874.

[35] S. Osaki, K. Yamamoto, A. Kajiwara, M. Murata, Evaluation of the resistance of spider silk to ultraviolet irradiation, Polym. J. 36 (2004) 623–627.

[36] G.B. Perea, C. Solanas, G.R. Plaza, G.V. Guinea, I. Jorge, J. Vázquez, J.M. Pérez Mateos, N. Marí-Buyé, M. Elices, J. Pérez-Rigueiro, Unexpected behavior of irradiated spider silk links conformational freedom to mechanical performance, Soft Matter 11 (2015) 4868–4878.

[37] K. Hafner, D. Montag, H. Maeser, C. Peng, W.R. Marcotte, D. Dean, M.S. Kennedy, Evaluating adhesion and alignment of dental pulp stem cells to a spider silk substrate for tissue engineering applications, Mater. Sci. Eng. C 81 (2017) 104–112.

[38] N. Kono, H. Nakamura, M. Mori, Y. Yoshida, R. Ohtoshi, A.D. Malay, D. A. Pedrazzoli Moran, M. Tomita, K. Numata, K. Arakawa, Multicomponent nature underlies the extraordinary mechanical properties of spider dragline silk, Proc. Natl. Acad. Sci. 118 (2021), e2107065118.

[39] A. Sponner, W. Vater, S. Monajembashi, E. Unger, F. Grosse, K. Weisshart, Composition and hierarchical organisation of a spider silk, PLoS One 2 (2007), e998.

[40] K. Augsten, P. Mühlig, C. Herrmann, Glycoproteins and skin-core structure in Nephila clavipes spider silk observed by light and electron microscopy, Scanning 22 (2000) 12–15.

[41] T. Lefevre, M.E. Rousseau, M. Pezolet, Protein secondary structure and orientation in silk as revealed by Raman spectromicroscopy, Biophys. J. 92 (2007) 2885–2895.

[42] T. Lefevre, F. Paquet-Mercier, J.F. Rioux-Dube, M. Pezolet, Review structure of silk by raman spectromicroscopy: from the spinning glands to the fibers, Biopolymers 97 (2012) 322–336.

[43] C. Riekel, M. Burghammer, M. Rosenthal, Nanoscale X-ray diffraction of silk fibers, Frontiers in Materials 6 (2019).

[44] R.J. Young, C. Holland, Z. Shao, F. Vollrath, Spinning conditions affect structure and properties of Nephila spider silk, MRS Bull. 46 (2021) 915–924.

[45] K. Bekelis, S. Missios, R.J. Spinner, Falls and peripheral nerve injuries: an age-dependent relationship, J. Neurosurg. 123 (2015) 1223–1229.

[46] K.R. Jessen, R. Mirsky, The repair Schwann cell and its function in regenerating nerves, J. Physiol. 594 (2016) 3521–3531.

[47] M.G. Burnett, E.L. Zager, Pathophysiology of peripheral nerve injury: a brief review, Neurosurg. Focus. 16 (2004) E1.

[48] J.W. Kuhbier, C. Allmeling, K. Reimers, A. Hillmer, C. Kasper, B. Menger, G. Brandes, M. Guggenheim, P.M. Vogt, Interactions between spider silk and cells–NIH/3T3 fibroblasts seeded on miniature weaving frames, PLoS One 5 (2010) e12032.

[49] J. Pérez-Rigueiro, M. Elices, G.R. Plaza, J. Rueda, G.V. Guinea, Fracture surfaces and tensile properties of UV-irradiated spider silk fibers, J. Polym. Sci. B Polym. Phys. 45 (2007) 786–793.

[50] P.M. Cunniff, S.A. Fossey, M.A. Auerbach, J.W. Song, D.L. Kaplan, W.W. Adams, R. K. Eby, D. Mahoney, D.L. Vezie, Mechanical and thermal properties of dragline silk from the spider Nephila clavipes, Polym. Adv. Technol. 5 (1994) 401–410.

[51] European Parliament, C.o.t.E.U., Directive 2010/63/EU of the European Parliament and of the council of 22 September 2010 on the protection of animals used for scientific purposes (text with EEA relevance), Off. J. Eur. Union 53 (L 276) (2010) 33–79.

[52] M. Haertinger, T. Weiss, A. Mann, A. Tabi, V. Brandel, C. Radtke, Adipose stem cell-derived extracellular vesicles induce proliferation of Schwann cells via internalization, Cells 9 (2020) 163–179.

[53] Z. Shao, F. Vollrath, J. Sirichaisit, R.J. Young, Analysis of spider silk in native and supercontracted states using Raman spectroscopy, Polymer 40 (1999) 2493–2500.

[54] G. Ashiotis, A. Deschildre, Z. Nawaz, J.P. Wright, D. Karkoulis, F.E. Picca, J. Kieffer, The fast azimuthal integration Python library: pyFAI, J. Appl. Crystallogr. 48 (2015) 510–519.

[55] M. Newville, T. Stensitzki, D.B. Allen, M. Rawlik, A. Ingargiola, A. Nelson, LMFIT: Non-linear Least-Square Minimization and Curve-Fitting for Python, Astrophysics Source Code Library, 2016 pp.ascl-1606.

[56] H.P. Klug, L.E. Alexander, X-Ray Diffraction Procedures: For Polycrystalline and Amorphous Materials, 2nd edition, Wiley Interscience, New York, 1974.

[57] J.O. Warwicker, Comparative studies of fibroins: II. The crystal structures of various fibroins, J. Mol. Biol. 2 (1960) 350–IN351.

[58] B. Madsen, Z.Z. Shao, F. Vollrath, Variability in the mechanical properties of spider silks on three levels: interspecific, intraspecific and intraindividual, Int. J. Biol. Macromol. 24 (1999) 301–306.
[59] P.C. Austin, Balance diagnostics for comparing the distribution of baseline covariates between treatment groups in propensity-score matched samples, Stat. Med. 28 (2009) 3083–3107.
[60] F. Bretz, T. Hothorn, P. Westfall, in: C.A. Hall (Ed.), Multiple Comparisons Using R, CRC, New York, 2011.
[61] K. Lau, B. Akhavan, M.S. Lord, M.M. Bilek, J. Rnjak-Kovacina, Dry surface treatments of silk biomaterials and their utility in biomedical applications, ACS Biomaterials Science & Engineering 6 (2020) 5431–5452.
[62] C. Riekel, M. Burghammer, T.G. Dane, C. Ferrero, M. Rosenthal, Nanoscale structural features in major Ampullate spider silk, Biomacromolecules 18 (2017) 231–241.
[63] R.E. Marsh, R.B. Corey, L. Pauling, An investigation of the structure of silk fibroin, Biochim. Biophys. Acta 16 (1955) 1–34.
[64] C. Riekel, C. Bränden, C. Craig, C. Ferrero, F. Heidelbach, M. Müller, Aspects of X-ray diffraction on single spider fibers, Int. J. Biol. Macromol. 24 (1999) 179–186.
[65] R. Ene, C. Krywka, S.-G. Kang, P. Papadopoulos, M. Burghammer, E. Di Cola, M. Müller, F. Kremer, Structure changes in Nephila dragline: the influence of pressure, Polymer 53 (2012) 5507–5512.
[66] R. Fraser, T.P. MacRae, Conformation in Fibrous Proteins and Related Synthetic Polypeptides, Academic Press, New York, 1973.
[67] G. Greco, H. Mirbaha, B. Schmuck, A. Rising, N.M. Pugno, Artificial and natural silk materials have high mechanical property variability regardless of sample size, Sci. Rep. 12 (2022) 3507.
[68] B. Madsen, F. Vollrath, Mechanics and morphology of silk drawn from anesthetized spiders, Naturwissenschaften 87 (2000) 148–153.
[69] J. Sirichaisit, V.L. Brookes, R.J. Young, F. Vollrath, Analyis of structure/property relationships in silkworm (Bombyx mori) and spider dragline (Nephila edulis) silks using Raman spectroscopy, Biomacromolecules 4 (2003) 387–394.
[70] Y.H. Lu, H. Lin, Y.Y. Chen, C. Wang, Y.R. Hua, Structure and performance ofBombyx mori silk modified with nano-TiO2 and chitosan, Fibers and Polymers 8 (2007) 1–6.
[71] T. Kornfeld, J. Nessler, C. Helmer, R. Hannemann, K.H. Waldmann, C.T. Peck, P. Hoffmann, G. Brandes, P.M. Vogt, C. Radtke, Spider silk nerve graft promotes axonal regeneration on long distance nerve defect in a sheep model, Biomaterials 271 (2021), 120692.
[72] S. Houshyar, A. Bhattacharyya, R. Shanks, Peripheral nerve conduit: materials and structures, ACS Chem. Neurosci. 10 (2019) 3349–3365.
[73] C. Chen, X. Kong, I.-S. Lee, Modification of surface/neuron interfaces for neural cell-type specific responses: a review, Biomed. Mater. 11 (2015), 014108.
[74] C. Simitzi, A. Ranella, E. Stratakis, Controlling the morphology and outgrowth of nerve and neuroglial cells: the effect of surface topography, Acta Biomater. 51 (2017) 21–52.
[75] J.A. Mitchel, D. Hoffman-Kim, Cellular scale anisotropic topography guides Schwann cell motility, PLoS One 6 (2011), e24316.
[76] Q. Min, D.B. Parkinson, X.-P. Dun, Migrating Schwann cells direct axon regeneration within the peripheral nerve bridge, Glia, n/a.
[77] L. Ning, H. Sun, T. Lelong, R. Guilloteau, N. Zhu, D.J. Schreyer, X. Chen, 3D bioprinting of scaffolds with living Schwann cells for potential nerve tissue engineering applications, Biofabrication 10 (2018), 035014.
[78] S. Gnavi, B.E. Fornasari, C. Tonda-Turo, G. Ciardelli, M. Zanetti, S. Geuna, I. Perroteau, The influence of electrospun fibre size on Schwann cell behaviour and axonal outgrowth, Mater. Sci. Eng. C 48 (2015) 620–631.
[79] C. Thamm, T. Scheibel, Recombinant production, characterization, and Fiber spinning of an engineered short major Ampullate Spidroin (MaSp1s), Biomacromolecules 18 (2017) 1365–1372.
[80] G. Rosso, I. Liashkovich, P. Young, D. Rohr, V. Shahin, Schwann cells and neurite outgrowth from embryonic dorsal root ganglions are highly mechanosensitive, Nanomedicine 13 (2017) 493–501.
[81] Y. Gu, Y. Ji, Y. Zhao, Y. Liu, F. Ding, X. Gu, Y. Yang, The influence of substrate stiffness on the behavior and functions of Schwann cells in culture, Biomaterials 33 (2012) 6672–6681.
[82] N. Chaudhry, C. Bachelin, V. Zujovic, M. Hilaire, K.T. Baldwin, R.M. Follis, R. Giger, B.D. Carter, A. Baron-Van Evercooren, M.T. Filbin, Myelin-associated glycoprotein inhibits Schwann cell migration and induces their death, J. Neurosci. 37 (2017) 5885–5899.
[83] K. Yazawa, A.D. Malay, H. Masunaga, K. Numata, Role of skin layers on mechanical properties and supercontraction of spider dragline silk fiber, Macromol. Biosci. 19 (2019), e1800220.
[84] B. An, M. Tang-Schomer, W. Huang, J. He, J. Jones, R.V. Lewis, D.L. Kaplan, Physical and biological regulation of neuron regenerative growth and network formation on recombinant dragline silks, Biomaterials 48 (2015) 137–146.